Materials Today Electronics 16 (2026) 100215

Contents lists available at ScienceDirect

Materials Today Electronics

journal homepage: www.elsevier.com/locate/mtelec

Full Length Article

Nitrogen-enabled amorphous stabilization of high-mobility in-rich IGO via PEALD for uniform and reliable oxide TFTs

YuJin Yang [a,1], Sang-Hyun Kim [b,1], Tae Heon Kim [c], Jeong-Su Song [b], Sun Myung Lee [a], Ki-Cheol Song [c,d], Yeonhee Lee [d], Yoon-Seo Kim [e,*], Jin-Seong Park [a,b,c,*]

[a] Department of Semiconductor Engineering, Hanyang University, 222 Wangsimni-ro, Seongdong-gu, Seoul 04763, Republic of Korea
[b] Department of Display Science and Engineering, Hanyang University, 222 Wangsimni-ro, Seongdong-gu, Seoul 04763, Republic of Korea
[c] Division of Materials Science and Engineering, Hanyang University, Seoul 04763, Republic of Korea
[d] Advanced Analysis and Data Center, Korea Institute of Science and Technology (KIST), 5, Hwarang-ro, Seongbukgu, Seoul 02792, Republic of Korea
[e] imec, Kapeldreef 75, B-3001 Leuven, Belgium

ARTICLE INFO

Keywords:
Plasma-enhanced atomic layer deposition
Indium gallium oxide
Amorphous oxide semiconductor
Nitrogen doping
Thin-film transistors

ABSTRACT

Indium-based oxide semiconductors are promising materials for next-generation display backplanes owing to their high intrinsic carrier mobilities. However, their strong tendency to crystallize and excessive carrier generation often reduce the device uniformity and reliability. In this study, nitrogen-doped indium-rich indium gallium oxide (IGO) thin films were fabricated via plasma-enhanced atomic layer deposition (PEALD) using N_2O plasma. Nitrogen incorporation effectively suppressed crystallization and passivated the oxygen vacancies, which produced stable amorphous films, even after annealing at 400 °C. The prepared IGO thin-film transistors (TFTs) exhibited a high mobility of 55.3 $cm^2/V{\cdot}s$, a normally off threshold voltage of 0.7 V, and a steep subthreshold swing of 85 mV/dec. Nitrogen doping increased the threshold voltage uniformity by 90% (standard deviation = 42 mV). Moreover, the bias-stress stability improved by 79% under positive bias temperature stress and 83% under negative bias temperature stress, with small shifts in the threshold voltage of 0.23 and 0.04 V, respectively. These improvements were attributed to the formation of a grain boundary-free amorphous network and the reduction of deep-level traps through controlled nitrogen doping. This study demonstrates that PEALD-based nitrogen incorporation offers a simple and scalable route for realizing high-mobility, uniform, and reliable amorphous oxide TFTs for future display technologies.

1. Introduction

The emergence of high-resolution and large-area next-generation displays has positioned oxide semiconductor (OS) thin-film transistors (TFTs) as the next stage in the evolution of display backplane technologies [1–3]. The active materials used in display backplanes have evolved from amorphous silicon (a-Si) to low-temperature polycrystalline silicon (LTPS) and, more recently, to OSs. Owing to their low-temperature processability and excellent film uniformity across large substrates, a-Si TFTs have been used extensively in liquid crystal displays [4]. However, their low electron mobility (~1 $cm^2/V{\cdot}s$) limits their use in high-speed and high-resolution applications [5]. Therefore, LTPS technology, which offers a higher mobility (~80 $cm^2/V{\cdot}s$) than a-Si, has been introduced to overcome this limitation [6]. However, LTPS requires expensive laser annealing processes and suffers from limited uniformity across large substrates owing to its crystalline nature [7,8]. Consequently, OSs have emerged as an attractive alternative to Si-based materials. Unlike a-Si, OSs exhibit high electron mobility (~10 $cm^2/V{\cdot}s$) even in the amorphous phase, allowing fast operation without crystallization [9,10]. This enables excellent large-area uniformity and process scalability. As display technologies continue to demand higher resolutions and larger panel sizes, the development of amorphous OSs with enhanced mobility (>50 $cm^2/V{\cdot}s$) and superior reliability has become increasingly important [11,12].

Owing to the self-limiting nature of the chemical reactions, atomic layer deposition (ALD) is well-suited for the development of high-quality OSs with high mobility and excellent reliability [13–16]. Compared to conventional physical deposition methods, ALD minimizes damage and

* Corresponding authors.
E-mail addresses: yoon-seo.kim@imec.be (Y.-S. Kim), jsparklime@hanyang.ac.kr (J.-S. Park).
[1] These authors contributed equally to this work.

https://doi.org/10.1016/j.mtelec.2026.100215
Received 25 December 2025; Received in revised form 22 February 2026; Accepted 23 March 2026
Available online 26 March 2026

impurities during film growth, thereby contributing to improved device performance [17,18]. Moreover, it can be used to precisely control the film composition and thickness, which makes it ideal for engineering complex multicomponent oxide systems [19]. Among the various ALD techniques, plasma-enhanced ALD (PEALD) increases these advantages by activating surface reactions through plasma energy, thereby enabling low-temperature and high-throughput processing suitable for large-area display manufacturing [20,21]. Moreover, PEALD can be tuned via various process parameters, including the plasma power, gas species, and chamber pressure, which allows advanced film crystallization control and intentional doping [22,23]. Recently, reactive gases have been introduced during ALD as a means to incorporate anions [24,25]. Such reactive gas engineering exhibits characteristics distinct from those of conventional oxidants, enabling enhanced tunability in device properties. For example, Kim et al. demonstrated that nitrogen incorporation using N_2O plasma enables selective doping at the In, Ga, and Zn sites in IGZO films, with substitution being particularly effective at the Ga sites, which suppresses carrier generation by reducing the number of oxygen vacancies (V_O) and passivating sub-gap states [26]. This approach increases the electrical stability and highlights the potential of PEALD-based reactive gas engineering as a powerful route for tailoring the structural and electronic properties of OSs.

ALD-based research has mainly focused on In_2O_3-based OSs to achieve higher carrier mobilities and superior electrical performances [27,28]. However, pristine In_2O_3 inherently suffers from excessive carrier generation owing to the abundant V_O and the strong tendency toward crystallization [29,30]. Therefore, gallium has been incorporated to suppress the formation of V_O in In_2O_3, thereby limiting excessive carrier generation [31,32]. However, indium-rich indium gallium oxide (IGO) tends to crystallize easily, and carrier control remains challenging, even in the presence of Ga [33,34]. The formation of polycrystalline phases introduces numerous grain boundaries that reduce film uniformity, complicate device property control, and reduce electrical stability during long-term operation [35,36]. Various doping strategies have been investigated to suppress crystallization in indium-rich IGO, which readily exhibits crystalline behavior.

Doping can suppress nucleation by inducing lattice distortion, modifying the bond energy, or changing the nucleation energy barrier [37]. For example, cation doping with elements that have large ionic radii or different valence states can hinder nucleation by inducing lattice distortions or modifying the local bonding environment, thereby stabilizing the amorphous phase [38]. However, cation incorporation may negatively affect the electronic structure by directly changing the conduction band configuration, which often reduces the carrier transport. Therefore, anion doping has attracted attention as an approach that can suppress crystallization and reduce the number of V_O without disturbing the conduction path. This strategy offers a promising route toward achieving high-mobility and reliable indium-rich OSs.

In this study, we developed an indium-rich OS film with high mobility while maintaining an amorphous phase. The amorphous structure was realized by incorporating nitrogen into the film via PEALD using nitrogen-containing reactant gases. The incorporated nitrogen perturbed the bond length and angle of the metal-oxygen network, which induced local strain and lattice distortions and effectively suppressed crystallization. Consequently, the nitrogen-doped indium-rich IGO films maintained their amorphous structure up to 400 °C. Moreover, the reduced concentration of V_O allowed precise carrier control, enabling enhancement-mode operation alongside a high mobility of >50 $cm^2/V{\cdot}s$. Furthermore, V_O passivation and crystallization suppression led to remarkable improvements in the positive bias temperature stress (PBTS), negative bias temperature stress (NBTS), and negative bias illumination stress (NBIS) stabilities. In practice, amorphous IGO films with incorporated nitrogen exhibit high mobility, excellent reliability, and outstanding uniformity. Therefore, our results indicate that these films are promising candidates for next-generation large-area display applications.

2. Experimental

2.1. Fabrication of IGO thin films

IGO thin films were deposited onto SiO_2 (100 nm)/heavily doped p-type Si substrates or Si substrates via PEALD. The deposition was performed in a temporal wafer-type capacitively coupled plasma reactor with a chamber size of 15 cm × 15 cm. The metal precursors used as the indium and gallium sources were [3-(dimethylamino)propyl]dimethylindium (DADI) and trimethylgallium (TMGa), respectively. The DADI was maintained at 55 °C, whereas the TMGa was cooled to 15 °C. The reaction gases were either a 1:1 mixture of O_2 (99.999%) and Ar (99.999%) supplied at a flow rate of 200 sccm or a 1:1 mixture of N_2O (99.999%) and Ar under the same conditions. All the PEALD process parameters (pulse/purge time, working pressure, and temperature) except for the reaction gas composition and plasma power were fixed across all the tests. Argon was used as both the carrier and purge gas at a constant flow rate of 200 sccm. The deposition temperature and chamber pressure were fixed at 200 °C and 1.2 Torr, respectively, and the plasma exposure time was fixed at 1 s for all conditions. The plasma power was set to 100 W when using the O_2/Ar mixture, and to 100, 150, or 200 W when using the N_2O/Ar mixture to achieve different levels of nitrogen incorporation. To minimize the influence of impurities such as carbon, excluding the effect of nitrogen incorporation, the deposition was carried out within a plasma power range that ensured complete decomposition of the metal cation precursors. As shown in Figs. 1a and 1c, the super-cycle was designed with an In-to-Ga sub-cycle ratio of 12:2, which resulted in an overall In:Ga cation ratio of 4:1. The film uniformity was evaluated at nine different points within the chamber, arranged in a pattern similar to that of the flower points on a Go board.

2.2. Characterization of IGO thin films

The film thickness, growth per cycle (GPC), and refractive index (RI) were measured using spectroscopic ellipsometry (Elli-SE(UV)-FM8, Ellipso Technology). The oxygen and nitrogen bonding states were analyzed using X-ray photoelectron spectroscopy (XPS, K-alpha+, Thermo Fisher Scientific Co.) with an Al-Kα (1486.6 eV) source. The cation composition was determined using X-ray fluorescence (XRF, ARL QUANT'X EDXRF, Thermo Fisher Scientific Co.). The film crystallinity and degree of crystal alignment were characterized using grazing incidence X-ray diffraction (GIXRD, SmartLab, RIGAKU) at the Hanyang Center for Research Facilities in Seoul. The nitrogen amount was analyzed using Secondary Ion Mass Spectrometry (D-SIMS, IMS 7F-Auto, CAMECA) at the KIST in Seoul. D-SIMS analysis was conducted using a Cs^+ ion source with an impact energy of 6 keV to detect negative ions. The film density was measured using X-ray reflectivity (XRR, SmartLab, Rigaku) with Cu-Kα radiation (wavelength: 1.54 Å). The surface morphology was examined using atomic force microscopy (AFM, NX20, Park Systems).

2.3. Device fabrication

The effects of nitrogen doping on the device characteristics were investigated by fabricating top-gate bottom-contact IGO TFTs using PEALD-deposited IGO as the active layer. IGO TFTs were fabricated on heavily doped p-type Si substrates with a thermally grown SiO_2 layer (100 nm). All the layers of all the devices were deposited in the same PEALD chamber to ensure uniform processing conditions. Each layer was patterned using photolithography followed by wet etching. The source and drain electrodes were formed by depositing a 100 nm-thick indium tin oxide (ITO) layer via RF sputtering. The active layer was deposited to a thickness of 10 nm under O_2 plasma and N_2O plasma according to the process described above. The channel width and length of the active layer were set to 40 and 20 μm, respectively. The gate insulator was deposited as a 20 nm-thick Al_2O_3 layer via PEALD. Al_2O_3

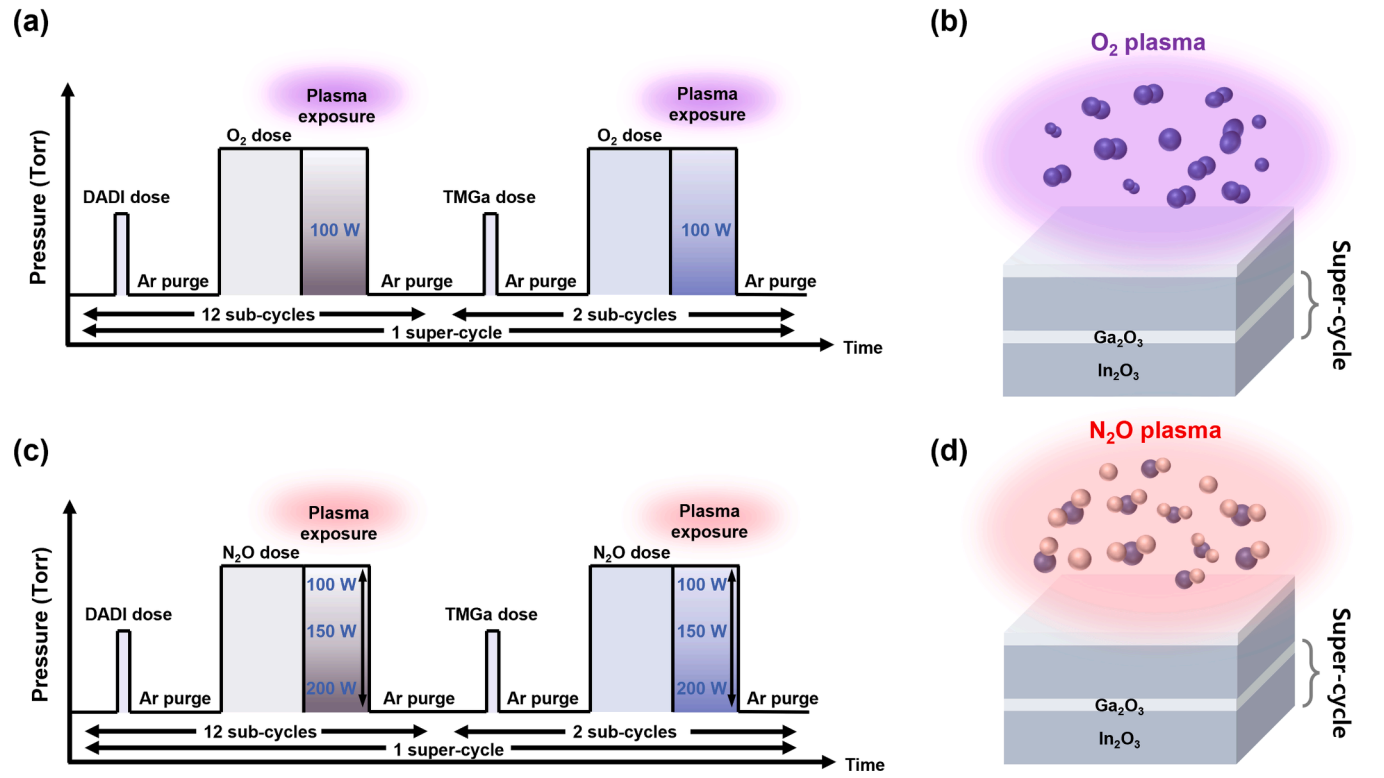

Fig. 1. PEALD process schemes for IGO deposition using different plasma reactants. (a) IGO deposition sequence using O_2 plasma in a super-cycle process. (b) Schematic showing the film growth mechanism with O_2 plasma as the reactant. (c) IGO deposition sequence using N_2O plasma in a super-cycle process. (d) Schematic showing the film growth mechanism with N_2O plasma as the reactant.

was grown at 200 °C using a trimethylaluminum (TMA) precursor and O_2 reactant gas at a plasma power of 100 W. The deposition sequence was as follows: TMA pulse (0.2 s), Ar purge (10 s), O_2 pulse (10 s), O_2 plasma (1 s), Ar purge (15 s). The gate electrode was formed by depositing a 100 nm thick ITO layer that was identical to that of the source/drain electrodes. After fabrication, all the devices were post-annealed at 400 °C for 3 h in a dry air atmosphere (O_2 21%/N_2 79%, purity: 99.999%).

2.4. Device characterization

All devices were evaluated using a Keithley 4200 semiconductor parameter analyzer. The μ_{FE} was calculated using the equation $\mu_{FE} = Lg_{m,max}/(WC_{ox}V_{DS})$, where $g_{m,max}$ is the maximum transconductance; W and L are the channel width and length, respectively; C_{ox} is the gate insulator capacitance per unit area, and V_{DS} is the drain voltage, which was fixed at 0.1 V. The value of C_{ox} was calculated using the equation $\varepsilon_r\varepsilon_0/T_{ox}$, where ε_r is the dielectric constant of the gate insulator, ε_0 is the permittivity of free space, and T_{ox} is the thickness of the gate insulator. Moreover, g_m was determined using the equation dI_D/dV_{GS}, where V_{GS} is the gate voltage and I_D is the drain current. Here, I_D was measured by performing a double sweep of V_{GS} from −5 to 5 V with a step size of 0.05 V. The value of V_{th} was determined via linear extrapolation from the linear regions of the transfer curves. The SS was derived from the slope of the V_{GS}–log(I_D) curve, where SS = $dV_{GS}/d\log(I_D)$. The electrical characteristics of 25 TFTs were evaluated, and their average values and standard deviations were extracted. PBTS and NBTS tests were performed under electrical fields of +2 and −2 MV/cm, respectively, at 60 °C for 3600 s to evaluate the device stability. NBIS measurements were conducted under an electrical field of 2 MV/cm with a light intensity of 1000 lx. The hydrogen resistance of the devices was evaluated by conducting an additional annealing step at 400 °C for 1800 s in a hydrogen-forming-gas atmosphere (H_2 4% + N_2 96%). After this treatment, the values of μ_{FE} and V_{th} were determined again using the same methods described above, and the changes were compared.

3. Results and discussion

IGO thin films were deposited by alternately stacking InO_x and GaO_y layers using PEALD, as shown in Figs. 1a and 1c. Each super-cycle consisted of two sub-cycles: (1) InO_x deposition (In precursor dose-purge-O_2 or N_2O gas dose-O_2 or N_2O plasma-purge), and (2) GaO_y deposition (Ga precursor dose-purge-O_2 or N_2O gas dose-O_2 or N_2O plasma-purge). We investigated the effects of incorporating nitrogen into the IGO by depositing the films using O_2 and N_2O plasma reactant gases, as shown in Figs. 1b and 1d Because N_2O contains both oxygen and nitrogen, it participates directly in surface reactions during PEALD, which enables uniform nitrogen incorporation throughout the film [39, 40]. The N_2O plasma power was varied from 100 to 200 W in 50 W increments to control the degree of nitrogen incorporation, and O_2 plasma at 100 W was used as the reference condition without nitrogen. An In:Ga composition ratio of 4:1 was achieved by setting the number of sub-cycles for In and Ga to 12 and 2, respectively. As shown in Figure S1, all the O_2 and N_2O plasma conditions produced a consistent composition ratio of 4:1, indicating that the relative deposition rates of In and Ga were unaffected by the plasma power. This confirms that the plasma power acted solely as a variable for controlling the degree of nitrogen incorporation without affecting the intrinsic compositional stability of the PEALD process.

Fig. 2a shows the GPC and RI of the IGO films deposited using O_2 plasma (100 W) and N_2O plasma (100, 150, and 200 W). The GPC per super-cycle was 10.42 Å/cycle for O_2 plasma at 100 W, whereas it decreased to 8.05 Å/cycle for N_2O plasma at 100 W, and then linearly increased to 8.54 and 8.92 Å/cycle as the plasma power increased to 150 and 200 W, respectively. Unlike O_2 plasma, N_2O plasma generates oxygen radicals (O•), nitrogen radicals (N•), and NO-related species [41,

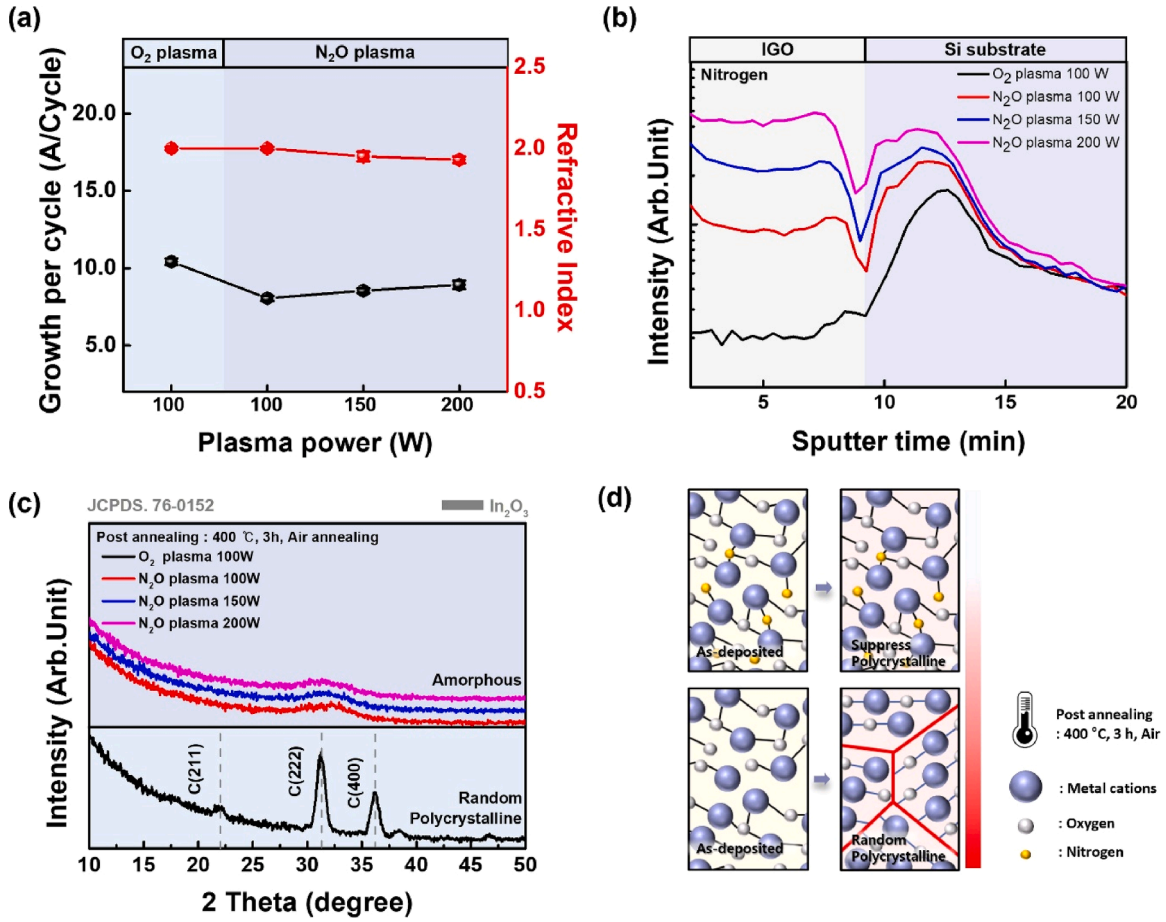

Fig. 2. Growth and structural characteristics of IGO films deposited via PEALD under different plasma conditions. (a) GPC and RI as a function of plasma power. (b) D-SIMS depth profiles confirming that nitrogen was incorporated into the films prepared using N_2O plasma. (c) XRD spectra after post-annealing showing that nitrogen incorporation suppressed crystallization. (d) Schematic showing the structural evolution mechanism where nitrogen stabilized the amorphous network and suppressed crystallization.

42]. Therefore, the reduced GPC can be attributed to the lower concentration of oxygen radicals and the participation of nitrogen radicals in surface reactions, in which some oxidation is replaced by nitridation. In other words, nitrogen radicals replace some of the metal-oxygen bonds with metal-nitrogen (In-N, Ga-N) or mixed (In-O-N) bonds, which reduces the oxidation efficiency and the adsorption of the precursor on the -OH-terminated surface, which reduces the growth rate. D-SIMS was performed to verify the nitrogen incorporation, as shown in Fig. 2b Compared with the O_2 plasma film, the intensity of the nitrogen peak was much higher in the N_2O plasma films, and it increased linearly as the plasma power increased. This confirms that the nitrogen content in the IGO films can be tuned by adjusting the plasma power, and that nitrogen radicals actively participate in the formation of metal-nitrogen and mixed In-O-N bonds during PEALD.

Fig. 2c shows the XRD spectra of the IGO films after annealing at 400 °C, which illustrates the different crystallization behaviors during the O_2 plasma and N_2O plasma processes. The diffraction peaks were indexed to the (222), (400), and (411) planes of bixbyite In_2O_3, respectively (JCPDS No.76–0152). The O_2 plasma IGO film exhibited pronounced crystallization with distinct (222), (400), and (411) diffraction peaks, whereas the N_2O plasma IGO film retained an amorphous structure after annealing. All the films were amorphous prior to annealing, and these differences became evident after annealing at 400 °C. Furthermore, the IGO films deposited under N_2O plasma at 150 and 200 W maintained their amorphous phases after annealing at 600 °C, as shown in Figure S2. Even at 100 W, the N_2O plasma IGO film exhibited a lower XRD peak intensity than the O_2 plasma counterpart, indicating that nitrogen effectively suppresses crystallization even at high temperatures. As shown in Figure S3, indium-rich IGO (e.g., In:Ga $\geq$ 3:1) without nitrogen was fully crystallized after annealing, because the indium-rich matrix favored the thermodynamically stable bixbyite cubic phase of In_2O_3 [43]. However, when nitrogen was incorporated, crystallization was suppressed. As shown in Fig. 2d, nitrogen incorporation perturbed the bond angles and lengths within the metal-oxygen network, which induced local strain and lattice distortion [37,38]. In addition, the formation of the InN and GaN phases further disrupted the order of the IGO matrix. The accumulation of these localized distortions inhibited the development of long-range crystalline order, which stabilized the amorphous phase.

Additional experiments were conducted using O_2 plasma at 100–200 W to exclude the possibility that the crystallization behavior was affected solely by the plasma power. As shown in Figure S4, all the O_2 plasma films crystallized regardless of the plasma power, and the diffraction peaks were similar to those observed at 100 W. Therefore, crystallization was suppressed owing to nitrogen incorporation, rather than variations in plasma power.

These differences in the crystallization behavior also resulted in variations in the film density and surface roughness. Figure S5 shows the XRR and film densities of the IGO films deposited under different plasma conditions. The highest film density was obtained using O_2 plasma at 100 W, and the density gradually decreased as the N_2O plasma power increased. This can be attributed to the fact that nitrogen has a lower atomic mass than oxygen and metal cations. After thermal annealing, the film density of the N_2O plasma films increased slightly, whereas that

of the O_2 plasma film showed a more pronounced increase. This difference occurred because the N_2O plasma films maintained an amorphous structure even after annealing, whereas the O_2 plasma film crystallized, which resulted in densification.

Figure S6 shows AFM images of the IGO films under each plasma condition. The O_2 plasma film exhibited the highest surface roughness with a root mean square value of 0.181 nm, which was attributed to grain boundary formation during crystallization. By contrast, the N_2O plasma films exhibited smoother surfaces owing to their amorphous nature. The RMS roughness values for the N_2O plasma films were 0.162 nm (100 W), 0.139 nm (150 W), and 0.141 nm (200 W). Furthermore, when the plasma power increased from 100 to 150 W, the roughness decreased, from 0.162 to 0.139 nm, which was likely because the nitrogen passivated the surface dangling bonds and other defect sites. However, the roughness increased slightly at 200 W, which can be attributed to surface damage induced by plasma bombardment effects at higher plasma powers [44].

The chemical bonding states of the IGO films with incorporated nitrogen were analyzed using XPS at the O 1 s and N 1 s spectra, as shown in Fig. 3. The O 1 s spectra consisted of three components: metal-oxygen bonds (M-O, 529.6 eV), oxygen-related defects (O_{def}, 531.1 eV), and oxygen impurities (532.2 eV), as shown in Figs. 3a, 3b, and S7 [35,45]. As the N_2O plasma power increased, the oxygen-related defect component decreased continuously from 21.49% under O_2 plasma to 16.89%, 15.89%, and 15.43% under N_2O plasma at 100, 150, and 200 W, respectively. This reduction in the oxygen-related defect component may be attributed to both the oxidizing species with increasing plasma power and the passivation effect induced by nitrogen incorporation. However, Kim et al. reported that, in PEALD-based oxide semiconductors, the higher binding energy region increased with increasing plasma power [46]. This suggests that the oxygen-related defect component in PEALD-based oxide semiconductors is not significantly affected by plasma power alone, and that the primary cause is the passivation effect resulting from increased nitrogen incorporation. Therefore, compared with the O_2 plasma process, the N_2O plasma process offers a distinct advantage in enabling more precise regulation of oxygen-related defects. Correspondingly, the oxygen-impurity component increased from 7.84% to 8.55%, 10.96%, and 14.00%. The oxygen-impurity component generally represents bonding with light elements such as hydrogen, carbon, nitrogen and excess oxygen. Auger electron spectroscopy (AES) depth profiles (Figure S8) confirmed that carbon was not present in any of the IGO films, indicating that the metal cation precursors decomposed completely during PEALD. As the N_2O plasma power increases, the possible formation of excess oxygen species, such as interstitial or weakly bonded oxygen, cannot be completely excluded. However, the total oxygen concentration remained within a narrow range (51.5–52 at%) across all plasma conditions, within the experimental error. In addition, despite the higher oxygen radical reactivity in the O_2 plasma process, the O_2 plasma films exhibited a lower O-impurity fraction. Therefore, it is difficult to attribute the primary variation in the O-impurity component to excess oxygen species. Furthermore, as shown in Figure 3(c), a clear evolution of O—N bonding is observed in the N 1 s spectra. This trend is consistent with the change in the O-impurity peak in the O 1 s spectra, suggesting that the O-impurity component is more closely correlated with O—N bonding formation. Owing to the absence of carbon, the limited contribution of excess oxygen species, and the minimal contribution of hydrogen to the O 1 s peak, the oxygen-impurity component can be reasonably interpreted as being primarily associated with O—N bonding resulting from nitrogen incorporation into the IGO films. These results suggest that nitrogen incorporation effectively passivates deep-level traps, reducing O_{def} and increasing the O—N bonding fraction.

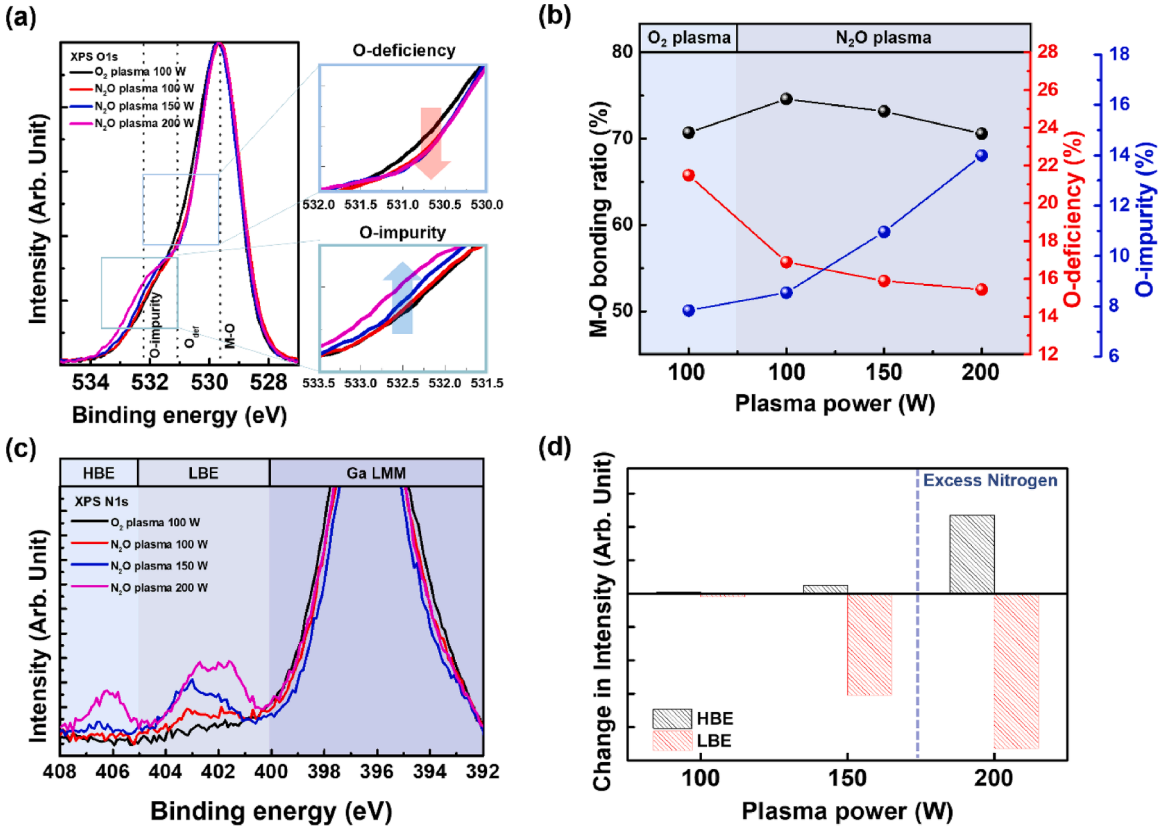

Fig. 3. Chemical bonding characteristics of PEALD-deposited IGO films under different plasma conditions. (a) XPS O 1 s spectra of the IGO films as a function of the plasma power. (b) Deconvolution of the O 1 s spectra into three bonding components: M-O, O-deficiency, and O—N bonding. (c) XPS N 1 s spectra of the IGO films as a function of the plasma power. (d) Changes in the intensity of the N 1 s subpeaks corresponding to HBE and LBE after thermal annealing.

The N 1 s spectra (Fig. 3c) were consistent with the O 1 s results. The N 1 s peak exhibited a high-binding-energy (HBE) subpeak at approximately 407 eV and a low-binding-energy (LBE) subpeak centered at approximately 403 eV, which both correspond to NO_x-related bonding states [39]. Unlike metal-nitrogen bonding, which was observed as a peak at approximately 396 eV, O—N bonding was observed at higher N 1 s binding energies because the highly electronegative oxygen greatly reduces the electron density around the nitrogen, leaving it in a more positively charged state. The metal-nitrogen peak could not be distinguished because it overlapped with the Ga LMM Auger peak.

The LBE subpeak increased linearly with the plasma power, whereas the HBE subpeak increased sharply at 200 W. As shown in Figure S9, before annealing, the N 1 s spectra were dominated by the LBE component, which increased with the plasma power, whereas the HBE component was approximately zero. After thermal annealing, the LBE intensity decreased owing to nitrogen diffusion, which was accompanied by a slight increase in the HBE component. Fig. 3d shows a comparison of the changes in the N 1 s subpeaks before and after annealing. At 100 W, both components remained approximately unchanged. At 150 W, the LBE intensity decreased slightly, whereas the HBE intensity only showed a minor increase. By contrast, at 200 W, the HBE sub-peak intensity increased significantly, indicating excessive nitrogen incorporation under strong plasma conditions [39]. During annealing, this excess nitrogen either diffused outward or transformed into NO_x-related HBE species. These NO_x-related changes are consistent with the O 1 s spectra, where stronger O—N bonding was observed as the N_2O plasma power increased.

In addition to bonding with oxygen, nitrogen in the IGO films also forms bonds with metal cations. Figure S10 presents the XPS Ga 2p and In 3d spectra. In the Ga 2p spectrum, the Ga-O bond is located at approximately 1117.8 eV, whereas a lower binding energy component at approximately 1117.1 eV corresponds to Ga-N bonding. Similarly, in the In 3d spectrum, the In-O bond appears at approximately 444.4 eV, while the In-N component is observed at a lower binding energy of approximately 443.6 eV. Although the changes are subtle, the intensities of the Ga-N and In-N peaks increase as the nitrogen incorporation

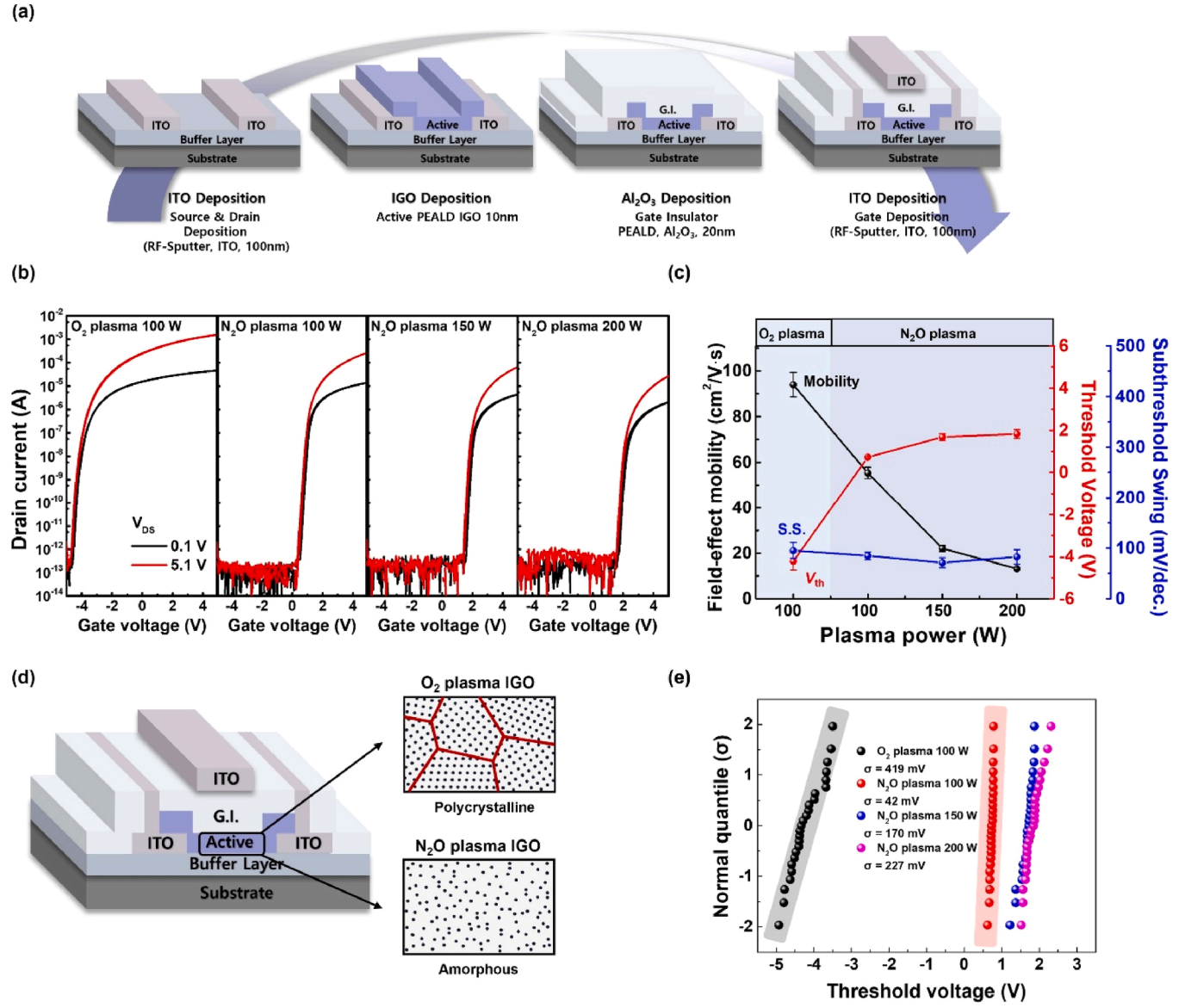

Fig. 4. Electrical characteristics of oxide TFTs using PEALD-deposited IGO as the active layer. (a) Schematic showing the device architecture with a flow chart detailing the fabrication process of nitrogen-incorporated top-gate bottom-contact oxide TFTs. (b) Transfer curves of the TFTs as a function of the plasma power. (c) Averaged device parameters (μ_{FE}, V_{th}, and SS) obtained from 25 devices under each plasma condition. (d) Schematic showing the crystalline phase formation under O_2 plasma and amorphous structure retention under N_2O plasma. (e) Normal probability plot of V_{th} extracted from 25 devices.

increases with N_2O plasma. These results indicate that nitrogen not only bonds with oxygen but also forms metal-nitrogen bonds within the IGO films, contributing to the formation of M-O-N-M network configurations. Therefore, nitrogen in the IGO films can passivate oxygen-related defects such as V_O or exist in the form of O—N and M-N bonding states. The presence of these various nitrogen configurations within the IGO films induces local strain and lattice distortion in the metal-oxygen network, thereby suppressing crystallization.

Nitrogen incorporation via PEALD using N_2O plasma effectively suppressed the crystallization of indium-rich IGO, resulting in oxide TFTs with superior switching characteristics. The optimized device fabricated under 100 W N_2O plasma exhibited a high field-effect mobility (μ_{FE}) of 55.3 $cm^2/V{\cdot}s$, showing normally off operation with a threshold voltage (V_{th}) of 0.7 V and a steep subthreshold swing of 85 mV/dec. Fig. 4a shows a schematic of the top-gate bottom-contact TFT and the stepwise fabrication process. The devices were fabricated on heavily doped p-type Si substrates with thermally grown SiO_2 layers, and all deposition steps were conducted below 200 °C. ITO source/drain electrodes were deposited by radio frequency (RF) sputtering to form an ohmic contact with the IGO active layer. The IGO films were deposited via PEALD using O_2 or N_2O plasma (100–200 W), as shown in Fig. 1, to investigate the effects of nitrogen incorporation. The gate insulator was also deposited at 200 °C with a plasma power of 100 W and a plasma exposure time of 1 s to minimize thermal and plasma-induced damage to the underlying active layer.

As shown in Fig. 4b, the transfer characteristics varied systematically with the plasma conditions, and the averaged μ_{FE}, V_{th}, and subthreshold swing (SS) values from 25 devices are summarized in Fig. 4c and Table S1. Figure S10 shows the output characteristics for each plasma condition. Under O_2 plasma at 100 W, the device exhibited a high μ_{FE} of 94.0 $cm^2/V{\cdot}s$ and a highly negative V_{th} of −4.2 V. This was attributed to excessive carrier generation in the indium-rich crystalline film, where partial crystallization produced a high carrier density and interface traps at the grain boundaries, which led to a degraded SS of 95.3 mV/dec [47–49]. When N_2O plasma at 100 W was applied, the carrier density was effectively suppressed and a high μ_{FE} of 55.3 $cm^2/V{\cdot}s$ was maintained. Consequently, V_{th} shifted positively to 0.7 V, achieving a normally off characteristic where the device remained completely off at a bias of 0 V, which ensures a lower leakage current and greater thermal stability.

The amorphous nature of the IGO film with incorporated nitrogen eliminated the grain boundaries and reduced the interface trap density, thereby increasing the SS to 85.0 mV/dec [40]. As the N_2O plasma power increased to 150 and 200 W, the reduction in V_O, together with O—N bonds acting as trap states and carrier scattering induced by O—N-related structures, led to decreases in μ_{FE} to 22.1 and 13.2 $cm^2/V{\cdot}s$, respectively, while V_{th} shifted positively to 1.63 and 1.83 V, respectively. This confirmed that nitrogen incorporation effectively modulated the carrier concentration. The SS increased further to 71.0 mV/dec at 150 W owing to enhanced trap passivation; however, it decreased slightly to 82.7 mV/dec at 200 W owing to plasma-induced interfacial damage [46,50]. This is consistent with the surface roughness data obtained from the AFM measurements. These results demonstrate that nitrogen incorporation through N_2O plasma enables precise carrier and V_{th} control, thereby enhancing the overall switching performance of indium-rich IGO TFTs.

The amorphous active layers in the TFTs exhibited excellent device-to-device uniformity [51,52]. Fig. 4d shows the crystallinity of the active layers under different plasma conditions. The O_2 plasma sample exhibited random polycrystalline characteristics owing to the indium-rich crystallization, whereas the N_2O plasma samples retained their amorphous nature. Fig. 4e shows the normal probability plot of V_{th}. The V_{th} distribution of the N_2O plasma at 100 W was considerably sharper than that of the O_2 plasma at 100 W. Random polycrystalline films typically exhibit significant device-to-device variations because the electrical characteristics depend on the grain size and orientation. As shown in Figure S12, the O_2 plasma devices exhibited a wide V_{th} distribution from −4.9 to −3.5 V with a large standard deviation of 419 mV. By contrast, the amorphous N_2O plasma devices showed an extremely narrow V_{th} range from 0.62 to 0.78 V and a significantly reduced deviation of 42 mV, corresponding to a 90% improvement in uniformity. However, excessive plasma power increased the variability owing to bombardment-induced damage. These results demonstrate that uncontrolled crystallization must be suppressed and the amorphous structure must be maintained to achieve highly uniform and reliable oxide TFTs. Stable nitrogen incorporation into IGO films enables high mobility, normally off characteristics, and excellent device-to-device uniformity, thereby resulting in superior performance among the reported oxide transistors, as shown in Table S2 of the benchmarking results [53–61].

Nitrogen improves the reliability of oxide TFTs by suppressing crystallization to maintain an amorphous structure and by passivating the V_O [62]. Figs. 5a and 5b show the evolution of the transfer characteristics of the IGO TFTs under a PBTS at an electric field of 2 MV/cm and a temperature of 60 °C, and the corresponding V_{th} shift as a function of the stress time, respectively. The TFT fabricated using O_2 exhibited a positive V_{th} shift of 1.10 V after 3600 s, whereas the TFT fabricated using N_2O plasma at 100 W showed a much smaller shift of 0.23 V, representing a 79.1% improvement in stability. Further increases in the plasma power to 150 and 200 W caused the V_{th} shift to increase again to 0.69 and 1.07 V, respectively.

As shown in Fig. 5c, these PBTS behaviors can be explained by differences in the structure and defect state of the active layer. In the O_2 plasma film, the indium-rich IGO exhibited randomly oriented polycrystalline phases containing grain boundaries that acted as defect sites for electron trapping under a positive gate bias, resulting in a positive V_{th} shift [35,63]. By contrast, the N_2O plasma films retained an amorphous microstructure without grain boundaries, which suppressed electron trapping and improved the stability. Furthermore, the nitrogen passivated oxygen-related defects, such as the V_O. Because the V_O are important electron-trapping sites under PBTS, reducing the number of V_O increases the reliability of the device [41,42,64]. However, at higher plasma powers, excessive N_2O exposure increased O—N bonding within the film. Such excessive O—N bonds can act as localized trap states, and plasma bombardment introduces additional interfacial disorder, which both contribute to the renewed V_{th} instability [65,66]. Therefore, moderate nitrogen incorporation is optimal for suppressing crystallization, reducing defect density, and passivating the V_O, ultimately improving the PBTS reliability.

Following the PBTS evaluation, further tests were conducted to ascertain the reliability of the devices in the off state under temperature and light stress conditions (NBTS and NBIS, respectively), and their resilience to hydrogen exposure. Fig. 6 shows the hydrogen resistance, reliability, and characteristics of the devices under NBTS and NBIS conditions. Figure S13a shows the evolution of the transfer characteristics under NBTS (−2 MV/cm, 60 °C). Fig. 6a shows the corresponding V_{th} shift. Similar to the PBTS, the O_2 plasma TFT exhibited a negative shift of 0.23 V, whereas the 100 W N_2O plasma TFT showed a substantially reduced shift of 0.04 V, corresponding to an 82.6% improvement in stability [67]. As the N_2O plasma power increased, the magnitude of the V_{th} shift increased, which is consistent with the trends observed for the PBTS. These behaviors can be explained by the presence or absence of grain boundaries and the extent of V_O passivation induced by nitrogen.

Figure S13b shows the transfer-curve variation under NBIS (−2 MV/cm, 1000 lx), and Fig. 6b shows the corresponding V_{th} evolution. Under light illumination, photo-generated electron-hole pairs were produced, and defects such as grain boundaries, V_O, and excessive O—N bonds acted as deep-level or tail-state traps. These trap sites captured holes generated by illumination, leading to a negative V_{th} shift and reduced reliability [68]. Therefore, as in PBTS and NBTS, the 100 W N_2O plasma film, where crystallization was effectively suppressed and the number of

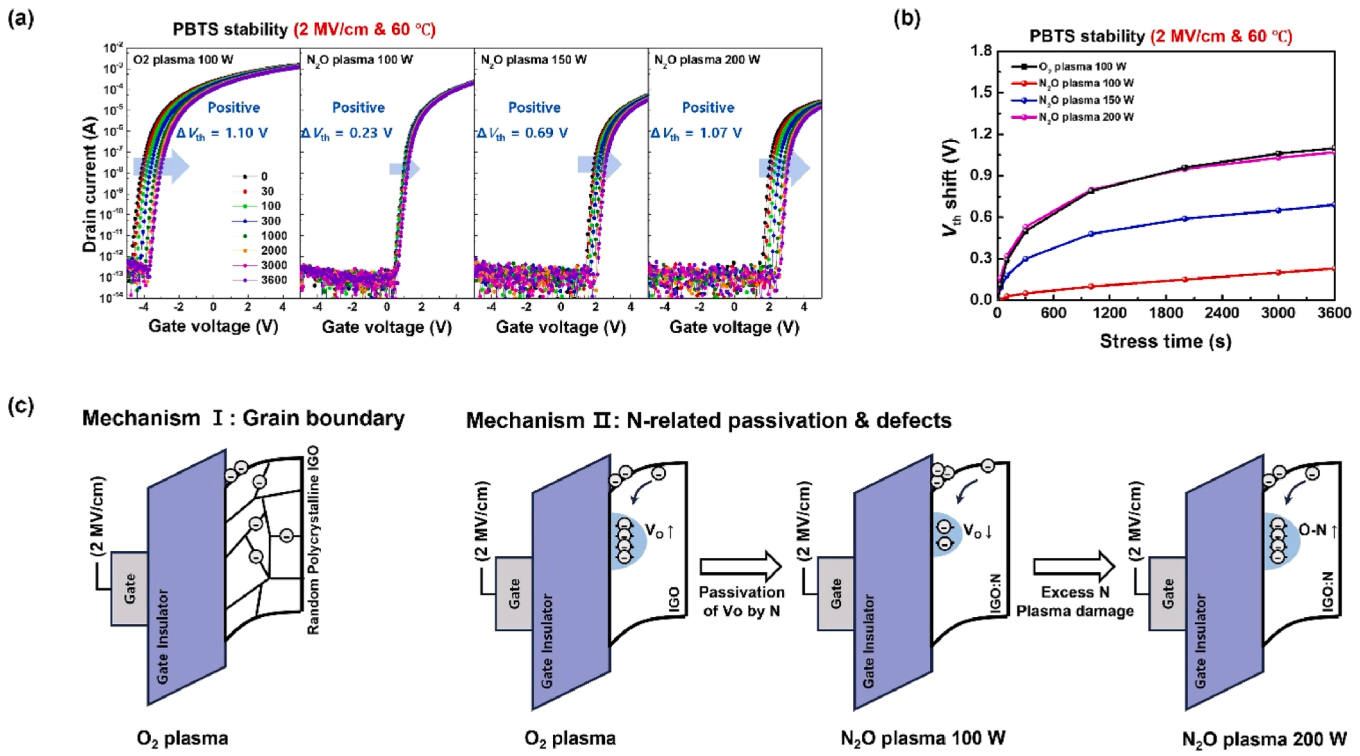

Fig. 5. Reliability characteristics of IGO TFTs with incorporated nitrogen. (a) Evolution of transfer curves under PBTS (2 MV/cm, 60 °C, 3600 s) for different plasma conditions. (b) Variation in V_{th} under PBTS as a function of the stress time. (c) Schematic showing the reliability mechanism under different plasma conditions.

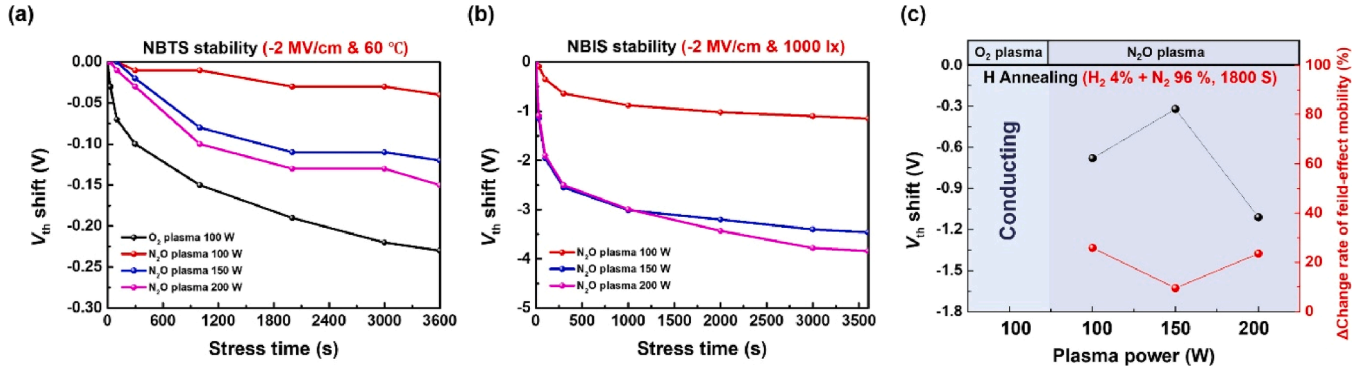

Fig. 6. Reliability and hydrogen resistance characteristics of IGO TFTs with incorporated nitrogen. (a) V_{th} under NBTS (−2 MV/cm, 60 °C, 3600 s) as a function of stress time. (b) V_{th} under NBIS (−2 MV/cm, 1000 lx, 3600 s) as a function of stress time. (c) Changes in the device characteristics (μ_{FE} and V_{th}) after forming-gas annealing (H_2 4% + N_2 96%) for 1800 s.

V_O was reduced, exhibited superior NBIS stability. By contrast, higher plasma powers caused increased carrier trapping owing to structural disorder and plasma-induced damage.

Hydrogen resistance testing was performed to evaluate the functional role of nitrogen within the active layer because nitrogen incorporation can modulate hydrogen-related reactions by suppressing the formation of O—H bonds through N—H interaction pathways. Fig. 6c shows the variations in μ_{FE} and V_{th} before and after forming-gas annealing (H_2 4% + N_2 96%, 1800 s), and Figure S14 shows the transfer characteristics of the TFTs after annealing. For the O_2 plasma TFT, hydrogen incorporation led to the formation of O—H bonds and donor-like hydrogen states, which resulted in an increased electron density and degraded switching behavior [12,69]. By contrast, the 100 W N_2O plasma TFT exhibited a V_{th} shift of −0.68 V and a 25.9% increase in μ_{FE}, indicating improved hydrogen resistance as O—N bonding limited the formation of O—H bonds [70,71]. As the plasma power increased to 150 W, the O—N bonding strength was further increased owing to the hydrogen resistance, which resulted in a smaller V_{th} shift of −0.32 V and a 9.6% increase in μ_{FE}. However, at 200 W, excessive nitrogen incorporation reduced the hydrogen-trapping capability, which led to a V_{th} shift of −1.11 V and a 23.6% increase in μ_{FE}, suggesting that the hydrogen resistance was reduced [70,71]. Therefore, the incorporation of nitrogen into the active layer via PEALD effectively suppresses crystallization in indium-rich materials and controls excess carriers, thereby enhancing the switching characteristics, uniformity, and overall device stability.

4. Conclusion

In this study, the amorphous indium-rich IGO channels fabricated via PEALD enabled the realization of high-mobility (>50 $cm^2/V{\cdot}s$) oxide TFTs exhibiting excellent switching characteristics, device uniformity, and reliability. Nitrogen incorporated by the N_2O plasma during PEALD effectively suppressed crystallization and passivated the V_O. In turn, this

stabilized the carrier concentration in the TFTs and enabled a normally off operation with a V_{th} of approximately 0.7 V. Despite moderate carrier suppression, a high μ_{FE} of approximately 55 $cm^2/V{\cdot}s$ was maintained, demonstrating the intrinsic potential of amorphous IGO. Nitrogen incorporation also enhanced both the device-to-device uniformity and bias-stress stability. Compared with the O_2 plasma condition, the V_{th} uniformity of the amorphous N_2O plasma IGO TFTs was improved by 90%, achieving a standard deviation as low as 42 mV owing to the suppression of random polycrystallinity. Under PBTS, the V_{th} shift was reduced by 79.1% relative to O_2 plasma devices, with a V_{th} shift of only 0.23 V, indicating enhanced reliability arising from the elimination of grain boundaries and the passivation of deep-level traps. Overall, controlled nitrogen incorporation via PEALD provides an effective and scalable route for suppressing crystallization and regulating excess carriers, offering a promising approach for realizing high-performance and highly reliable amorphous indium-rich OSs for next-generation displays and electronic applications.

CRediT authorship contribution statement

YuJin Yang: Writing – review & editing, Writing – original draft, Investigation, Formal analysis, Data curation. **Sang-Hyun Kim:** Writing – review & editing, Writing – original draft, Investigation, Formal analysis, Data curation, Conceptualization. **Tae Heon Kim:** Writing – review & editing, Writing – original draft, Investigation, Data curation. **Jeong-Su Song:** Writing – review & editing, Writing – original draft, Methodology, Data curation. **Sun Myung Lee:** Writing – review & editing, Writing – original draft, Methodology, Data curation. **Ki-Cheol Song:** Writing – review & editing, Writing – original draft, Methodology, Formal analysis. **Yeonhee Lee:** Writing – review & editing, Writing – original draft, Methodology, Formal analysis. **Yoon-Seo Kim:** Writing – review & editing, Writing – original draft, Validation, Investigation, Conceptualization. **Jin-Seong Park:** Writing – review & editing, Writing – original draft, Supervision, Project administration, Investigation, Conceptualization.

Declaration of competing interest

The authors declare that they have no known competing financial interests or personal relationships that could have appeared to influence the work reported in this paper.

Acknowledgments

This work was supported by the National Research Foundation of Korea (NRF) (grant nos. RS-2023-00260527 and RS-2025-00557667), the Technology Innovation Program funded by the Korean Ministry of Trade Industry and Energy (MOTIE) (grant nos. RS-2025-02308064 and RS-2025-25454815); and the Korea Institute for Advancement of Technology (KIAT) grant funded by the Korean Ministry of Trade, Industry, and Energy (MOTIE) (grant no. RS-2024-00410066).

Supplementary materials

Supplementary material associated with this article can be found, in the online version, at doi:10.1016/j.mtelec.2026.100215.

Data availability

Data will be made available on request.

References

[1] K. Nomura, H. Ohta, A. Takagi, T. Kamiya, M. Hirano, H. Hosono, Room-temperature fabrication of transparent flexible thin-film transistors using amorphous oxide semiconductors, Nature 432 (2004) 488–492, https://doi.org/10.1038/nature03090.

[2] H. Hosono, Recent progress in transparent oxide semiconductors: materials and device application, Thin Solid Film. 515 (2007) 6000–6014, https://doi.org/10.1016/j.tsf.2006.12.125.

[3] E. Fortunato, P. Barquinha, R. Martins, Oxide semiconductor thin-film transistors: a review of recent advances, Adv. Mater. 24 (2012) 2945–2986, https://doi.org/10.1002/adma.201103228.

[4] M.J. Powell, Charge trapping instabilities in amorphous silicon-silicon nitride thin-film transistors, Appl. Phys. Lett. 43 (1983) 597–599, https://doi.org/10.1063/1.94399.

[5] J. Lih, C. Sung, C. Li, T. Hsiao, H. Lee, Comparison of a-Si and poly-Si for AMOLED displays, J. Soc. Inf. Disp. 12 (2004) 367–371, https://doi.org/10.1889/1.1847734.

[6] J.Y. Kwon, K.S. Son, J.S. Jung, T.S. Kim, M.K. Ryu, K.B. Park, B.W. Yoo, J.W. Kim, Y.G. Lee, K.C. Park, S.Y. Lee, J.M. Kim, Bottom-gate gallium indium zinc oxide thin-film transistor array for high-resolution AMOLED display, IEEE Electron. Dev. Lett. 29 (2008) 1309–1311, https://doi.org/10.1109/LED.2008.2006637.

[7] Y.G. Mo, M. Kim, C.K. Kang, J.H. Jeong, Y.S. Park, C.G. Choi, H.D. Kim, S.S. Kim, Amorphous-oxide TFT backplane for large-sized AMOLED TVs, J. Soc. Inf. Disp. 19 (2011) 16–20, https://doi.org/10.1889/jsid19.1.16.

[8] T. Kamiya, H. Hosono, Material characteristics and applications of transparent amorphous oxide semiconductors, NPG Asia Mater. 2 (2010) 15–22, https://doi.org/10.1038/asiamat.2010.5.

[9] J.S. Park, W.J. Maeng, H.S. Kim, J.S. Park, Review of recent developments in amorphous oxide semiconductor thin-film transistor devices, Thin Solid Film. 520 (2012) 1679–1693, https://doi.org/10.1016/j.tsf.2011.07.018.

[10] D.H. Lee, Y.J. Chang, G.S. Herman, C.H. Chang, A general route to printable high-mobility transparent amorphous oxide semiconductors, Adv. Mater. 19 (2007) 843–847, https://doi.org/10.1002/adma.200600961.

[11] J. Raja, K. Jang, C.P.T. Nguyen, J. Yi, N. Balaji, S.Q. Hussain, S. Chatterjee, Improvement of mobility in oxide-based thin film transistors: a brief review, Trans. Electr. Electron. Mater. 16 (2015) 234–240, https://doi.org/10.4313/TEEM.2015.16.5.234.

[12] Y.S. Kim, T. Hwang, H.J. Oh, J.S. Park, J.S. Park, Reliability engineering of high-mobility IGZO transistors via gate insulator heterostructures grown by atomic layer deposition, Adv. Mater. Interfac. 11 (2024) 2301097, https://doi.org/10.1002/admi.202301097.

[13] N.P. Dasgupta, H.-B.-R. Lee, S.F. Bent, P.S. Weiss, Recent advances in atomic layer deposition, Chem. Mater. 28 (2016) 1943–1947, https://doi.org/10.1021/acs.chemmater.6b00673.

[14] N.E. Richey, C. De Paula, S.F. Bent, Understanding chemical and physical mechanisms in atomic layer deposition, J. Chem. Phys. 152 (2020) 040902, https://doi.org/10.1063/1.5133390.

[15] J. Sheng, K.L. Han, T. Hong, W.H. Choi, J.S. Park, Review of recent on flexible oxide semiconductor thin film transistors based on atomic layer deposition processes, J. Semicond. 39 (2018) 011008, https://doi.org/10.1088/1674-4926/39/1/011008.

[16] J. Sheng, J.-H. Lee, W.-H. Choi, T. Hong, M. Kim, J.-S. Park, Review article: atomic layer deposition for oxide semiconductor thin film transistors: advances in research and development, J. Vac. Sci. Technol. A 36 (2018) 060801, https://doi.org/10.1116/1.5047237.

[17] M.H. Cho, H. Seol, A. Song, S. Choi, Y. Song, P.S. Yun, K.-B. Chung, J.U. Bae, K.-S. Park, J.K. Jeong, Comparative study on performance of IGZO transistors with sputtered and atomic layer deposited channel layer, IEEE Trans. Electron. Devic. 66 (2019) 1783–1788, https://doi.org/10.1109/TED.2019.2899586.

[18] Y.-S. Kim, H. Hong, T.H. Hong, S.-H. Choi, K.-B. Chung, J.-S. Park, Attaining quantitatively fewer defects in close-packed InGaZnO synthesized using atomic layer deposition, Appl. Surf. Sci. 664 (2024) 160242, https://doi.org/10.1016/j.apsusc.2024.160242.

[19] M.H. Cho, C.H. Choi, J.K. Jeong, Recent progress and perspectives on atomic-layer-deposited semiconducting oxides for transistor applications, J. Soc. Inf. Disp. 30 (2022) 175–197, https://doi.org/10.1002/jsid.1096.

[20] H. Kim, Characteristics and applications of plasma enhanced-atomic layer deposition, Thin Solid Film. 519 (2011) 6639–6644, https://doi.org/10.1016/j.tsf.2011.01.404.

[21] S.E. Potts, W. Keuning, E. Langereis, G. Dingemans, M.C.M. van de Sanden, W.M. M. Kessels, Low temperature plasma-enhanced atomic layer deposition of metal oxide thin films, J. Electrochem. Soc. 157 (2010) P66–P74, https://doi.org/10.1149/1.3428705.

[22] H.M. Kim, D.G. Kim, Y.S. Kim, M. Kim, J.S. Park, Atomic layer deposition for nanoscale oxide semiconductor thin film transistors: review and outlook, Int. J. Extrem. Manuf. 5 (2023) 012006, https://doi.org/10.1088/2631-7990/acb46d.

[23] A.J.M. Mackus, J.R. Schneider, C. Macisaac, J.G. Baker, S.F. Bent, Synthesis of doped, ternary, and quaternary materials by atomic layer deposition: a review, Chem. Mater. 31 (2019) 1142–1183, https://doi.org/10.1021/acs.chemmater.8b02878.

[24] R.W. Johnson, A. Hultqvist, S.F. Bent, A brief review of atomic layer deposition: from fundamentals to applications, Mater. Today 17 (2014) 236–246, https://doi.org/10.1016/j.mattod.2014.04.026.

[25] S.M. George, Atomic layer deposition: an overview, Chem. Rev. 110 (2010) 111–131, https://doi.org/10.1021/cr900056b.

[26] D.G. Kim, H. Choi, Y.S. Kim, D.H. Lee, H.J. Oh, J.H. Lee, J. Kim, S. Lee, B. Kuh, T. Kim, H.Y. Kim, J.S. Park, Selectively nitrogen doped ALD-IGZO TFTs with extremely high mobility and reliability, ACS Appl. Mater. Interfac. 15 (2023) 31652–31663, https://doi.org/10.1021/acsami.3c05678.

[27] H. Kumomi, K. Nomura, T. Kamiya, H. Hosono, Amorphous oxide channel TFTs, Thin Solid Film. 516 (2008) 1516–1522, https://doi.org/10.1016/j.tsf.2007.03.161.
[28] T.H. Hong, Y.S. Kim, S.H. Choi, J.H. Lim, J.S. Park, Exploration of chemical composition of In–Ga–Zn–O system via PEALD technique for optimal physical and electrical properties, Adv. Electron. Mater. 9 (2023) 2201208, https://doi.org/10.1002/aelm.202201208.
[29] P. Agoston, K. Albe, Thermodynamic stability, stoichiometry, and electronic structure of bcc-In_2O_3 surfaces, Phys. Rev. B 84 (2011) 045311, https://doi.org/10.1103/PhysRevB.84.045311.
[30] M.V. Hohmann, P. Goston, A. Wachau, T.J.M. Bayer, J. Brötz, K. Albe, A. Klein, Orientation dependent ionization potential of In_2O_3: a natural source for inhomogeneous barrier formation at electrode interfaces in organic electronics, J. Phys. 23 (2011) 334203, https://doi.org/10.1088/0953-8984/23/33/334203.
[31] S. Jeong, Y.G. Ha, J. Moon, A. Facchetti, T.J. Marks, Role of gallium doping in dramatically lowering amorphous-oxide processing temperatures for solution-derived indium zinc oxide thin-film transistors, Adv. Mater. 22 (2010) 1346–1350, https://doi.org/10.1002/adma.200902450.
[32] G.H. Kim, W.H. Jeong, H.J. Kim, Electrical characteristics of solutionprocessed InGaZnO thin film transistors depending on Ga concentration, Phys. Status Solidi A 207 (2010) 1677–1679, https://doi.org/10.1002/pssa.200983742.
[33] G.B. Kim, T. Kim, S.W. Bang, J.S. Hur, C.H. Choi, M.J. Kim, J.K. Jeong, Strong immunity to drain-induced barrier lowering in ALD-grown preferentially oriented indium gallium oxide transistors, ACS Appl. Mater. Interfac. 16 (2024) 23467–23475, https://doi.org/10.1021/acsami.3c18591.
[34] M.J. Kim, S.W. Bang, J.S. Hur, S.H. Yoon, C.H. Choi, S.W. Chung, J.E. Oh, Y. Kim, B.J. Park, J. Lee, H. Yang, D. Ha, M.H. Cho, J.K. Jeong, Growth of highly-ordered-crystalline indium-gallium-oxide thin-film via plasma-enhanced ALD for high performance top-gate field-effect transistors, Small Method 9 (2025) 2402070, https://doi.org/10.1002/smtd.202402070.
[35] J.S. Hur, M.J. Kim, S.H. Yoon, H. Choi, C.K. Park, S.H. Lee, M.H. Cho, B.J. Kuh, J. K. Jeong, High-performance thin-film transistor with atomic layer deposition (ALD)-derived indium-gallium oxide channel for back-end-of-line compatible transistor applications: cation combinatorial approach, ACS Appl. Mater. Interfac. 14 (2022) 48857–48867, https://doi.org/10.1021/acsami.2c13489.
[36] S.H. Choi, J.M. Sim, J. Shin, S.H. Ryu, T. Hwang, S.Y. Lim, H.J. Oh, J.H. Kwag, J. Y. Lee, K.C. Song, Y. Lee, M. Song, J. Kim, C.K. Park, Y.H. Song, J.S. Park, Unveiling the hybrid-channel (poly-Si/IGO) structure for 3D NAND flash memory for improving the cell current and GIDL-assisted erase operation, Small Struct. 6 (2025) 2400495, https://doi.org/10.1002/sstr.202400495.
[37] T. Wang, J.G. Ekerdt, Atomic layer deposition of lanthanum stabilized amorphous hafnium oxide thin films, Chem. Mater. 21 (2009) 3096–3101, https://doi.org/10.1021/cm9001064.
[38] J.F. Chien, C.H. Chen, J.J. Shyue, M.J. Chen, Local electronic structures and electrical characteristics of well-controlled nitrogen-doped ZnO thin films prepared by remote plasma in situ atomic layer doping, ACS Appl. Mater. Interfac. 4 (2012) 3471–3475, https://doi.org/10.1021/am300551y.
[39] S.H. Kim, Y.S. Kim, T. Hwang, T.H. Kim, H. Koo, J.S. Park, J.S. Park, Reliability improvement of high mobility oxide TFTs based on hydrogen-resistant PEALD Al2O3 gate insulators grown with N_2O plasma, ACS Appl. Mater. Interfac. 17 (2025) 14168–14178, https://doi.org/10.1021/acsami.4c18561.
[40] T.H. Kim, D.G. Kim, S.H. Kim, T.K. Kim, K.C. Song, Y. Lee, J.S. Park, Nitrogen doping strategy in SiO_2 insulators for stable and hydrogen-resistant ALD-IGZO TFTs, ACS Appl. Mater. Interfaces 17 (2025) 19928–19937, https://doi.org/10.1021/acsami.4c22748.
[41] K. Park, J.H. Kim, T. Sung, H.W. Park, J.H. Baeck, J. Bae, K.S. Park, S. Yoon, I. Kang, K.B. Chung, H.S. Kim, J.Y. Kwon, Highly reliable amorphous In-Ga-Zn-O thin-film transistors through the addition of nitrogen doping, IEEE Trans. Electron Devic. 66 (2019) 457–463, https://doi.org/10.1109/TED.2018.2881799.
[42] J. Raja, K. Jang, N. Balaji, J. Yi, Suppression of temperature instability in InGaZnO thin-film transistors by in situ nitrogen doping, Semicond. Sci. Technol. 28 (2013) 115010, https://doi.org/10.1088/0268-1242/28/11/115010.
[43] P. Ágoston, K. Albe, Ab initio modeling of diffusion in indium oxide, Phys. Rev. B 81 (2010) 195205, https://doi.org/10.1103/PhysRevB.81.195205.
[44] I.K. Oh, G. Yoo, C.M. Yoon, T.H. Kim, G.Y. Yeom, K. Kim, Z. Lee, H. Jung, C.W. Lee, H. Kim, H.B.R. Lee, Very high frequency plasma reactant for atomic layer deposition, Appl. Surf. Sci. 387 (2016) 109–117, https://doi.org/10.1016/j.apsusc.2016.06.048.
[45] S.H. Choi, T.H. Hong, S.H. Ryu, J.S. Park, Plasma-enhanced atomic-layer-deposited indium oxide thin film using a DMION precursor within a wide process window, Ceram. Int. 48 (2022) 27807–27814, https://doi.org/10.1016/j.ceramint.2022.06.083.
[46] Y.S. Kim, H.J. Oh, J. Kim, J.H. Lim, J.S. Park, Approaches for 3D integration using plasma-enhanced atomic-layer-deposited atomically-ordered InGaZnO transistors with ultra-high mobility, Small Methods 7 (2023) 2300549, https://doi.org/10.1002/smtd.202300549.
[47] J. Sheng, T.H. Hong, H.M. Lee, K.R. Kim, M. Sasase, J. Kim, H. Hosono, J.S. Park, Amorphous IGZO TFT with high mobility of 70cm^2/(Vs) via Vertical dimension control using PEALD, ACS Appl. Mater. Interfac. 11 (2019) 40300–40309, https://doi.org/10.1021/acsami.9b14310.
[48] T. Iwasaki, N. Itagaki, T. Den, H. Kumomi, K. Nomura, T. Kamiya, H. Hosono, Combinatorial approach to thin-film transistors using multicomponent semiconductor channels: an application to amorphous oxide semiconductors in In-Ga-Zn-O system, Appl. Phys. Lett. 90 (2007) 242114, https://doi.org/10.1063/1.2749177.
[49] H.J. Park, T. Kim, M.J. Kim, H. Lee, J.H. Lim, J.K. Jeong, Improvement in performance of indium gallium oxide thin film transistor via oxygen mediated crystallization at a low temperature of 200°C, Ceram. Int. 48 (2022) 12806–12812, https://doi.org/10.1016/j.ceramint.2022.01.151.
[50] T. Kamiya, K. Nomura, H. Hosono, Present status of amorphous In-Ga-Zn-O thin-film transistors, Sci. Technol. Adv. Mater. 11 (2010) 044305, https://doi.org/10.1088/1468-6996/11/4/044305.
[51] J.K. Jeong, The status and perspectives of metal oxide thin-film transistors for active matrix flexible displays, Semicond. Sci. Technol. 26 (2011) 034008, https://doi.org/10.1088/0268-1242/26/3/034008.
[52] X. Huang, K. Hikake, S.H. Kim, K. Sakai, Z. Li, T. Mizutani, T. Saraya, T. Hiramoto, T. Takahashi, M. Uenuma, Y. Uraoka, M. Kobayashi, High-field transport and statistical variability of nanosheet oxide semiconductor FETs with channel length scaling, IEEE Trans. Electron Devic. 71 (2024) 7509–7515, https://doi.org/10.1109/TED.2024.3473888.
[53] T.H. Hong, H.J. Jeong, H.M. Lee, S.H. Choi, J.H. Lim, J.S. Park, Significance of pairing In/Ga precursor structures on PEALD $InGaO_x$ thin-film transistor, ACS Appl. Mater. Interfaces 13 (2021) 28493–28502, https://doi.org/10.1021/acsami.1c06575.
[54] Z. Chen, H. Huang, H. He, S. Sun, B. Ye, D. Luo, X. Liu, X. Zou, B. Zou, Interface engineering for hysteresis-free, high-performance, and stable a-IGO thin-film transistors, IEEE Trans. Electron. Devic. 72 (2025) 2360–2364, https://doi.org/10.1109/TED.2025.3542750.
[55] J.H. Cho, J.W. Park, M. Nhut Le, S.B. Shin, W. Oh, M. Kim, M. Son, V. thu Cao, B. Lee, K. Min, M. Han, I.S. Kim, D. Son, C. Kim, A. Facchetti, H. Kang, M.G. Kim, Fiber laser-assisted room-temperature crystallization of solution-processed indium-rich IGO thin films for high-performance, high-reliability thin-film transistors, J. Mater. Chem. C 14 (2026) 855–862, https://doi.org/10.1039/d5tc02983j.
[56] S.H. Ryu, H.M. Kim, D.G. Kim, J.S. Park, Highly C-axis aligned ALD-InGaO channel improving mobility and thermal stability for next-generation 3D memory devices, Adv. Electron. Mater. 11 (2025) 2400377, https://doi.org/10.1002/aelm.202400377.
[57] D.G. Kim, M. Kim, D.H. Lee, S. Lee, J. Kho, Y. Kim, B. Kuh, H. Yanagi, K. Fukui, J. S. Park, Facile routes to enhance doping efficiency using nanocomposite structures for high-mobility and stable PEALD-ITGO TFTs, Appl. Surf. Sci. 665 (2024) 160370, https://doi.org/10.1016/j.apsusc.2024.160370.
[58] S.G. Jeong, H.J. Jeong, J.S. Park, Low subthreshold swing and high performance of ultrathin PEALD InGaZnO thin-film transistors, IEEE Trans. Electron. Devic. 68 (2021) 1670–1675, https://doi.org/10.1109/TED.2021.3062321.
[59] Y.S. Kim, D. Kim, K.C. Song, Y. Lee, H.S. Yoo, Y.J. Kim, J. Kim, J.S. Park, ALD reactivity-driven 2DEG-like interfacial conduction in nanolaminate InGaZnO transistors toward high-mobility and stable oxide electronics, Adv. Electron. Mater. 12 (2025) e00642,https://doi.org/10.1002/aelm.202500642.
[60] H.S. Choi, D.H. Han, H.W. Jeong, J. Kim, J. Kim, G.H. Park, Y.H. Cho, S.H. Kim, Y. Goh, W. Jung, D. Ha, Y.J. Chung, M.H. Park, High-performance annealing-free $InGaZnO_x$ thin film transistors by thermal ALD, Appl. Phys. Lett. 128 (2026) 043505, https://doi.org/10.1063/5.0299768.
[61] S. Lee, T. Lim, S. Priyadarshi, S. Lee, J. Sun, Y. Kim, J. Jang, Strong two-dimensional electron gas at crystalline and amorphous InGaSnO stack interface for high performance transistors with high temperature stability, Adv. Mater. Technol. 10 (2025) e00811,https://doi.org/10.1002/admt.202500811.
[62] N. Lv, Z. Wang, M. Du, H. Wang, D. Zhang, M. Wong, M. Wang, Effect of nitrogen doping on elevated-metal metal-oxide (EMMO) thin-film transistors, IEEE Trans. Electron Devic. 69 (2022) 4271–4276, https://doi.org/10.1109/TED.2022.3178966.
[63] S. Baang, H. Lee, X. Zhang, J. Park, W.P. Kim, Y.W. Ko, S.H. Piao, H.J. Choi, J. H. Kwon, J.H. Bae, Operational stability of solution-processed indium-oxide thin-film transistors: environmental condition and electrical stress, J. Korean Phys. Soc. 72 (2018) 151–158, https://doi.org/10.3938/jkps.72.151.
[64] Y.C. Cheng, S.P. Chang, S.J. Chang, Investigation of nitrogen doping effects on light-induced oxygen vacancy ionization and oxygen desorption in c-IGO TFTs, Mater. Res. Express 6 (2019) 106445,https://doi.org/10.1088/2053-1591/ab24a6.
[65] Y.-C. Cheng, S.-P. Chang, S.-J. Chang, T.-H. Cheng, Y.-L. Tsai, Y.-Z. Chiou, L. Lu, Stability improvement of nitrogen doping on IGO TFTs under positive gate bias stress and hysteresis test, ECS J. Solid State Sci. Technol. 8 (2019) Q3034–Q3040, https://doi.org/10.1149/2.0081907jss.
[66] Y.C. Cheng, S.P. Chang, I.C. Chen, Y.L. Tsai, T.H. Cheng, S.J. Chang, Polycrystalline In-Ga-O thin-film transistors coupled with a nitrogen doping technique for high-performance UV detectors, IEEE Trans. Electron Devic. 67 (2020) 140–145, https://doi.org/10.1109/TED.2019.2955758.
[67] C.H. Han, S.S. Kim, K.R. Kim, D.H. Baek, S.S. Kim, B.D. Choi, Effects of electron trapping and interface state generation on bias stress induced in indium-gallium-zinc oxide thin-film transistors, Jpn. J. Appl. Phys. 53 (2014) 08NG04,https://doi.org/10.7567/JJAP.53.08NG04.
[68] L.C. Liu, J.S. Chen, J.S. Jeng, Role of oxygen vacancies on the bias illumination stress stability of solution-processed zinc tin oxide thin film transistors, Appl. Phys. Lett. 105 (2014) 023509,https://doi.org/10.1063/1.4890579.
[69] H.Y. Noh, W.G. Lee, J.H. Cha, J.S. Kim, W.S. Yun, M.J. Lee, H.J. Lee, Hydrogen diffusion and its electrical properties variation as a function of the IGZO stacking

structure, Sci. Rep. 12 (2022) 19816, https://doi.org/10.1038/s41598-022-24212-7.

[70] G. Li, A. Abliz, L. Xu, N. André, X. Liu, Y. Zeng, D. Flandre, L. Liao, Understanding hydrogen and nitrogen doping on active defects in amorphous In-Ga-Zn-O thin film transistors, Appl. Phys. Lett. 112 (2018) 253504,https://doi.org/10.1063/1.5032169.

[71] A. Abliz, Q. Gao, D. Wan, X. Liu, L. Xu, C. Liu, C. Jiang, X. Li, H. Chen, T. Guo, J. Li, L. Liao, Effects of nitrogen and hydrogen codoping on the electrical performance and reliability of InGaZnO thin-film transistors, ACS Appl. Mater. Interfaces 9 (2017) 10798–10804, https://doi.org/10.1021/acsami.6b15275.